Robust control of gust-induced vibration of highly flexible aircraft

Tianyi He [a], Weihua Su [b,*]

[a] *Department of Mechanical and Aerospace Engineering, Utah State University, Logan, UT, 84322-4130, United States*
[b] *Department of Aerospace Engineering and Mechanics, The University of Alabama, Tuscaloosa, AL, 35487-0280, United States*

ARTICLE INFO

ABSTRACT

This paper mainly addresses the gust suppression and alleviation of highly flexible aircraft using the model predictive controller (MPC) based on linear parameter-varying (LPV) models. The dynamic behavior of highly flexible aircraft is modeled by a coupled nonlinear aeroelastic and flight dynamic formulation. Conventional trailing-edge flaps along the main wings and tails are deployed to provide the required loads for the wing vibration control and/or longitudinal flight attitude control of the slender vehicle. The coupled dynamic equations are performed with linearization and model reduction about a series of nonlinear equilibria to derive reduced-order LPV models. This work considers two quantities as the scheduling parameters in building the LPV models: the gust-induced angle of attack and the modal magnitude of wing deformation. With the reduced-order LPV model, MPC is designed to minimize the wing vibration and rigid-body motions excited by the time-domain Dryden gust perturbation. The proposed LPV modeling is capable of describing large wing deformations, and the LPV-MPC innovatively previews the scheduling parameter and gust disturbance in the prediction horizon. The closed-loop flight responses of a highly flexible aircraft with gust disturbance are presented in the numerical studies, which demonstrate the effectiveness of controlling coupled vibrations and rigid-body dynamics of such slender vehicles.

1. Introduction

In general, missions involving airborne intelligence, surveillance, and reconnaissance [1], as well as civilian atmospheric research [2], necessitate aircraft with high-aspect-ratio wings, resulting in highly flexible vehicle platforms. The primary reason behind this design is to enhance the aircraft's aerodynamic performance during the long-endurance flight, which can be achieved through high-aspect-ratio wings with lightweight, flexible structures. However, the inherent flexibility in the wing structures requires special design and analysis tools. Previous studies [3,4] have demonstrated that the slender wings of highly flexible aircraft may experience large deformations under normal operational loads, exhibiting geometrically nonlinear behavior. Consequently, the structural dynamic and aeroelastic characteristics of the aircraft can undergo significant changes due to the large wing deformation. Furthermore, highly flexible aircraft often exhibit coupling between the low-frequency elastic modes of their slender wings and the rigid-body motions of the entire aircraft [4–8]. Hence, a nonlinear aeroelastic solution, which can adequately account for the coupled ef-

fects of the large wing deformation and the aeroelastic/flight dynamic characteristics of the complete aircraft, is crucial to the research.

In fact, research on the structural dynamics and aeroelasticity of slender aerospace structures can be traced back to early studies on helicopter blades. Hodges and Dowell developed the twisted nonuniform beam theory [9] for slender rotor blades. This theory considered small strains and moderate deformations, neglecting third- and higher-order geometrically nonlinear terms. Subsequently, various geometrically nonlinear beam formulations have been established. Based on the choice of independent variables to represent the displacement field and the treatment of the beam reference line's rotation, beam theories can be classified as displacement-based formulations [10,11], mixed-form formulations [12,13], or strain/stress-based formulations [14]. In the mixed-form formulation [12], the rotation along the beam reference line was solved as independent degrees of freedom. Hodges [13] introduced an update where nodal velocities and beam curvatures were defined as the structural states of the beam. Once the direct solution of the beam rotation is not required, the mixed-form formulation reduces the computational cost associated with solving geometrically nonlinear

Nomenclature

$\mathbf{A}, \mathbf{B}, \mathbf{C}, \mathbf{G}$	system matrices of linearized state-space equation
B	body-fixed reference frame
$\mathbf{C}^{GB}$	rotation matrix from B frame to G frame
$\mathbf{F}_i$	matrices of inflow governing equation, $(i = 1, 2, 3)$
G	global (inertial) reference frame
H_w	transfer function of Dryden continuous gust
$\mathbf{K}$	generalized stiffness matrix
$\mathbf{M}$	generalized inertial matrix
$\bar{\mathbf{M}}, \bar{\mathbf{C}}, \bar{\mathbf{K}}$	inertial, damping, and stiffness matrices of linearized equation
N, N_t	prediction horizon and total simulation horizon
n	white noise
$\mathbf{p}$	position vector
Q, Q_f, R	tuning matrices of cost function for output and input, respectively
$\mathbf{R}$	generalized load vector
T	thrust force
$\mathbf{U}$	future control input over control horizon
$\mathbf{u}$	control input
w_g	single gust profile
$\mathbf{w}_g$	wing spanwise gust perturbation distribution

$\mathbf{x}$	state of linearized state-space system
$\mathbf{y}$	output of system
α_g	gust-induced angle of attack
$\boldsymbol{\beta}$	rigid-body velocity with translational $\mathbf{v}_B$ and rotational $\boldsymbol{\omega}_B$ components
$\delta_e, \delta_a, \delta_r$	deflections of elevator, aileron, and rudder, respectively
$\boldsymbol{\varepsilon}$	elastic strain vector
$\boldsymbol{\varepsilon}^0$	initial elastic strain vector
$\boldsymbol{\zeta}$	quaternion
$\boldsymbol{\eta}$	magnitude of linear mode shapes
Θ	the set of scheduling parameter θ
θ	generalized scheduling parameter
$\boldsymbol{\lambda}$	inflow states
$\boldsymbol{\Phi}$	linear mode shapes
$\boldsymbol{\Omega}_\zeta$	matrix for rigid-body orientation propagation equation

Subscript

d	discrete time
F, B	flexible and rigid-body components, respectively, of a matrix or vector
max, min	upper and lower bounds of control input, respectively

beams. Palacios et al. [15] extensively discussed these three types of beam formulations for analyzing structural, aeroelastic, and flight dynamic behavior in highly flexible aircraft.

Numerous studies have investigated the geometrically nonlinear aeroelasticity of highly flexible wings and aircraft. While not aiming to provide an exhaustive list, several notable works are discussed here. In early studies on the aeroelastic characteristics and control of highly flexible aircraft, linearized modes, including rigid-body modes, were employed to predict the aircraft's local stability under different flight conditions [16]. Drela [17] developed a comprehensive model for a complete flexible aircraft by representing it as an assembly of interconnected nonlinear beams coupled with a compressible vortex/source-lattice with wind-aligned trailing vorticity. This aeroelastic formulation is known as ASWING [18]. Hodges and his colleagues, coupling the mixed-form beam formulation with the finite-state inflow theory [19–21], developed a geometrically nonlinear aeroelastic formulation called NATASHA to study complete highly flexible aircraft [3,4,22]. Cesnik and his colleagues invented a strain-based beam theory. By coupling with the finite-state inflow aerodynamics, they developed the package UM/NAST [6–8] to study the nonlinear aeroelastic and flight dynamic behavior of highly flexible aircraft. The unsteady vortex-lattice method (UVLM) can be coupled with the geometrically nonlinear beam formulation [23] for enhanced aerodynamic fidelity with free-wake and 3D effects.

The highly flexible aircraft are usually vulnerable to external perturbations during the flight. A famous sample was the crash of the Helios Prototype [2], whose unstable phugoid mode was quickly excited by the air disturbance during a flight. The diverging motion then caused the increase of airspeed on the vehicle's solar panels and eventually broke the structure.

Various control algorithms have been developed for aircraft gust vibration control or gust load alleviation, such as adaptive feedforward control [24], LQG-based model predictive control (MPC) [25], incremental nonlinear dynamic inversion control [26], discrete-time H_∞ preview control [27], etc. Nonetheless, the vibration control and gust load alleviation of highly flexible vehicles remain open challenges, especially with geometrically nonlinear wing deformation excited by the gust disturbance. Haghighat et al. [28] applied the model predictive control for gust alleviation of highly flexible aircraft. Cook et al. [29] designed a robust controller based on linearized aeroelastic models,

highlighting the effectiveness of an H_∞ controller for a relatively large linearized system.

In order to further address the robust gust control of slender vehicles, this study proposes applying the MPC based on linear-parameter varying (LPV) models, considering control performance and robustness. LPV models have been utilized in various control studies within the aerospace domain. Spillman [30] conducted an early investigation on robust longitudinal flight control using LPV feedback. Barker and Balas [31] applied LPV models for gain-scheduling in flutter control of a wing section. Lind [32] employed the LPV approach to control the vibration of a flexible hypersonic vehicle. He et al. [33] developed an LPV controller for vibration suppression in a blended-wing-body aircraft. Snyder et al. [34] presented the design and analysis of an adaptive control architecture for LPV systems subject to time-varying parametric uncertainties and external disturbances. The LPV-MPC has been well embraced as an effective way to address the nonlinear systems [35–37]. Qu et al. [38] studied transition flight control for a tiltrotor eVTOL aircraft using LPV models. Iannelli et al. [39] developed a data-driven algorithm to construct low-order LPV models from trajectories of aeroservoelastic systems. Gu et al. [40] focused on turbo-fan engine acceleration control based on a data-driven LPV model, where the controller was designed using the MPC algorithm. Kapnopoulos and Alexandridis [41] investigated the tuning of a quadrotor trajectory-tracking system using cooperative particle swarm optimization-based model predictive control. More recently, Samsam and Chhabra [42] proposed a nonlinear model predictive control strategy for robust tracking of multi-impulse smooth transfer trajectories.

This study aims to achieve robust control of vibration suppression and gust alleviation for highly flexible aircraft against wind gusts. To accomplish this, LPV models will be developed based on a series of linearized and reduced-order models of flexible aircraft. These linearized models will vary with the scheduling parameter associated with gust excitation: gust-induced angle of attack and modal magnitude of wing deformation. Subsequently, an MPC controller will be designed based on the LPV models. The numerical result will demonstrate the effectiveness of LPV-based MPC in gust load alleviation for highly flexible wings and aircraft.

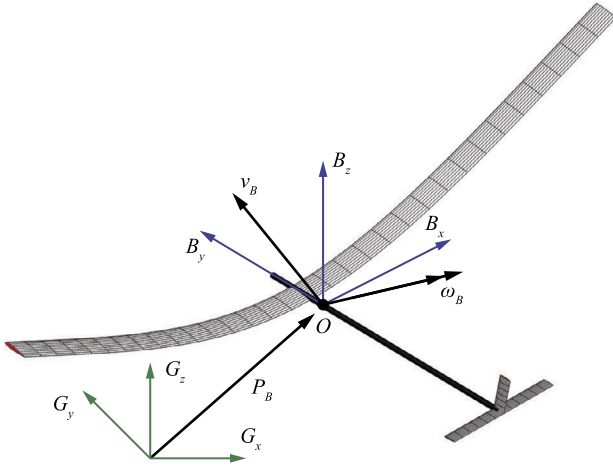The novelties and technical contributions of this proposed method are summarized as follows:

Fig. 1. Global and body frames defining the rigid-body motion of aircraft.

- For the first time, a novel LPV reduced-order model is established by considering the **modal magnitude** of wing deformation as the scheduling parameter. This approach allows the LPV model and control design to parameterize and handle the large wing deformation, which is a meaningful advance over the traditional aeroelastic models that are limited to the small deformation [33,43,44].
- The LPV-MPC proposed in this work innovatively previews the gust disturbance and gust-induced angle of attack in the prediction horizon to optimize control inputs. With state-of-the-art techniques of radar or Lidar [45], the wind gust ahead of an aircraft can be detected in real time. Therefore, the scheduling parameter of the angle of attack and gust disturbance can be previewed and updated in MPC. This feature differs from traditional robust MPC [35,46,47], which assumes unknown external disturbance and designs robust control for the worst case.
- In this study, the coupled wing vibrations and rigid-body dynamics are considered and controlled by the LPV-MPC. The flap, elevator, and thrust are used in feedback control for gust alleviation and vibration suppression simultaneously, which is different from the traditional works of flutter suppression [33,31]. The numerical results demonstrate that the proposed LPV-MPC can stabilize and minimize the perturbations of vibrations and rigid-body motions in the presence of gust disturbance. Furthermore, the controller can bring the flexible vehicle back to a steady state when the gust disturbance dies out.

2. Theoretical formulation

In this section, the geometrically nonlinear aeroelastic and flight dynamic formulation for highly flexible aircraft is briefly introduced first, followed by the development of LPV-MPC for the gust alleviation of such aircraft.

2.1. Nonlinear aeroelastic and flight dynamic formulation

As shown in Fig. 1, a body-fixed frame B is established in a global frame G is defined to describe the vehicle position and orientation. The body frame is a "'east-north-up" frame, with B_x pointing to the right and B_y pointing to the nose. The location of B can be arbitrary, yet it is convenient to establish the frame's origin in the symmetric plane of an aircraft. The rigid-body velocity of a free-flight vehicle is

$$\beta^T = \left\{ \mathbf{v}_B^T \quad \omega_B^T \right\} \tag{1}$$

where $\mathbf{v}_B$ and ω_B denote the translational and angular velocities of the B frame, respectively.
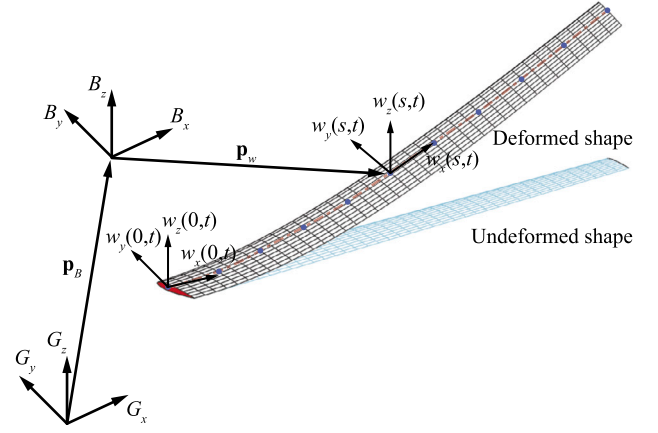

Fig. 2. Flexible lifting-surface frames within body frame.

By taking advantage of their geometry, highly flexible wings are modeled as slender beams that may exhibit large deformations during operation (see Fig. 2). Su and Cesnik introduced a nonlinear beam element [14] to model the geometrically nonlinear deformation of slender beams. In this formulation, the beam reference line's strain deformations (curvatures, ε) are the independent variables to describe the beam deformation.

By following the Principle of Virtual Work extended to dynamic systems, the dynamics of highly flexible aircraft in free flight can be described by

$$\mathbf{M}_{FF}(\varepsilon)\ddot{\varepsilon} + \mathbf{M}_{FB}(\varepsilon)\dot{\beta} + \mathbf{K}_{FF}\varepsilon = \mathbf{R}_F$$

$$\mathbf{M}_{BF}(\varepsilon)\ddot{\varepsilon} + \mathbf{M}_{BB}(\varepsilon)\dot{\beta} = \mathbf{R}_B$$

$$\dot{\zeta} = -\frac{1}{2}\mathbf{\Omega}_\zeta\zeta \tag{2}$$

$$\dot{\mathbf{p}}_B^G = \begin{bmatrix} \mathbf{C}^{GB} & \mathbf{0} \end{bmatrix}\beta$$

$$\dot{\lambda} = \mathbf{F}_1\lambda + \mathbf{F}_2\left\{ \begin{matrix} \dot{\varepsilon} \\ \beta \end{matrix} \right\} + \mathbf{F}_3\left\{ \begin{matrix} \ddot{\varepsilon} \\ \dot{\beta} \end{matrix} \right\}$$

where the components of the generalized inertia and stiffness matrices can be found in [7,8]. Unlike being presented in the references, the damping of the complete system is involved in the generalized load vector on the right-hand side of Eq. (2) for the convenience of writing the linearized equation of motion. The damping in this formulation involves the structural viscous damping proportional to the strain rate $\dot{\varepsilon}$, the centrifugal load, and the Coriolis effect. One can find more details about the inertia, damping, and stiffness terms in [7,8]. Overall, the generalized load vector also consists of the contributions of initial strain, gravity, aerodynamics, control load from trailing-edge flap deflections, and thrust force, i.e.,

$$\left\{ \begin{matrix} \mathbf{R}_F(\varepsilon,\dot{\varepsilon},\ddot{\varepsilon},\beta,\dot{\beta},\zeta,\lambda,\mathbf{u}) \\ \mathbf{R}_B(\varepsilon,\dot{\varepsilon},\ddot{\varepsilon},\beta,\dot{\beta},\zeta,\lambda,\mathbf{u}) \end{matrix} \right\} = \left\{ \begin{matrix} \mathbf{K}_{FF}\varepsilon^0 \\ \mathbf{0} \end{matrix} \right\} + \left\{ \begin{matrix} \mathbf{R}_F^{damp} \\ \mathbf{R}_B^{damp} \end{matrix} \right\} + \left\{ \begin{matrix} \mathbf{R}_F^{aero} \\ \mathbf{R}_B^{aero} \end{matrix} \right\}$$

$$+ \left\{ \begin{matrix} \mathbf{R}_F^{grav} \\ \mathbf{R}_B^{grav} \end{matrix} \right\} + \left\{ \begin{matrix} \mathbf{R}_F^{ctrl} \\ \mathbf{R}_B^{ctrl} \end{matrix} \right\}. \tag{3}$$

In Eq. (2), quaternion ζ describes the orientation of the B frame, $\mathbf{p}_B^G$ is the inertial position of the B frame resolved in the G frame, and $\mathbf{C}^{GB}$ is the rotation matrix from the body frame to the global frame [6]. In addition, the finite-state inflow theory is implemented for calculating the unsteady aerodynamic loads in Eq. (3), which also leads to the aerodynamic state governing equation in Eq. (2), where λ is the aerodynamic inflow state. More details of this theory were presented in [19,20]. Finally, the trailing-edge flap deflections, in addition to a single thrust force T applied at the origin of the body frame, are used as the command for control studies, i.e.,

$$\mathbf{u}^T = \left\{ \delta_e, \quad \delta_a, \quad \delta_r, \quad T \right\} \tag{4}$$

where δ_e, δ_a, δ_r are deflection angles of elevator, aileron, and rudder, respectively.

2.2. Gust model

In this study, the Dryden continuous gust model is implemented. The vertical gust velocity is obtained by filtering a Gaussian white noise signal $n(s)$ through a transfer function, i.e.,

$$w_g(s) = H_w(s)n(s). \tag{5}$$

Note that s here is the Laplace variable. According to the military specification MIL-F-8785C [48], the transfer function is

$$H_w(s) = \sigma_w \sqrt{\frac{L_w}{\pi U_\infty}} \frac{1 + \sqrt{3}\dfrac{L_w}{U_\infty}s}{\left(1 + \dfrac{L_w}{U_\infty}s\right)^2} \tag{6}$$

where U_∞ is the airspeed. L_w is the gust scale length, and σ_w is the gust intensity, both determined by the altitude. One may transform Eq. (5) to the time domain and integrate with the input white noise to obtain the gust velocity $w_g(t)$. The gust velocity, usually defined in the G frame, is uniformly applied on the wing surface, modifying the effective local angle of attack.

2.3. Linearized aeroelastic and flight dynamic equation

The Taylor's expansion is conducted on Eq. (2) about an equilibrium $(\varepsilon_0, \dot{\varepsilon}_0, \ddot{\varepsilon}_0, \beta_0, \dot{\beta}_0, \zeta_0, \dot{\zeta}_0, (p_B^G)_0, (\dot{p}_B^G)_0, \lambda_0, \dot{\lambda}_0)$ and the corresponding control input $(\mathbf{u}_0)$. It leads to a set of linearized equations, given by

$$\bar{\mathbf{M}}_{FF}\Delta\ddot{\varepsilon} + \bar{\mathbf{M}}_{FB}\Delta\dot{\beta} + \bar{\mathbf{C}}_{FF}\Delta\dot{\varepsilon} + \bar{\mathbf{C}}_{FB}\Delta\beta + \bar{\mathbf{K}}_{FF}\Delta\varepsilon =$$
$$\left.\frac{\partial\mathbf{R}_F^{\text{grav}}}{\partial\zeta}\right|_0 \Delta\zeta + \left.\frac{\partial\mathbf{R}_F^{\text{aero}}}{\partial\lambda}\right|_0 \Delta\lambda + \left.\frac{\partial\mathbf{R}_F^{\text{ctrl}}}{\partial\mathbf{u}}\right|_0 \Delta\mathbf{u} + \left.\frac{\partial\mathbf{R}_F^{\text{aero}}}{\partial\mathbf{w}_g}\right|_0 \mathbf{w}_g$$

$$\bar{\mathbf{M}}_{BF}\Delta\ddot{\varepsilon} + \bar{\mathbf{M}}_{BB}\Delta\dot{\beta} + \bar{\mathbf{C}}_{BF}\Delta\dot{\varepsilon} + \bar{\mathbf{C}}_{BB}\Delta\beta + \bar{\mathbf{K}}_{BF}\Delta\varepsilon =$$
$$\left.\frac{\partial\mathbf{R}_B^{\text{grav}}}{\partial\zeta}\right|_0 \Delta\zeta + \left.\frac{\partial\mathbf{R}_B^{\text{aero}}}{\partial\lambda}\right|_0 \Delta\lambda + \left.\frac{\partial\mathbf{R}_B^{\text{ctrl}}}{\partial\mathbf{u}}\right|_0 \Delta\mathbf{u} + \left.\frac{\partial\mathbf{R}_B^{\text{aero}}}{\partial\mathbf{w}_g}\right|_0 \mathbf{w}_g$$

$$\Delta\dot{\zeta} = -\frac{1}{2}\left.\frac{\partial(\boldsymbol{\Omega}_\zeta\zeta)}{\partial\beta}\right|_0 \Delta\beta - \frac{1}{2}\boldsymbol{\Omega}_\zeta\big|_0 \Delta\zeta$$

$$\Delta\dot{\mathbf{p}}_B^G = \left.\frac{\partial(\mathbf{C}^{GB}\mathbf{v}_B)}{\partial\zeta}\right|_0 \Delta\zeta + \begin{bmatrix}\mathbf{C}^{GB}\big|_0 & \mathbf{0}\end{bmatrix}\Delta\beta$$

$$\Delta\dot{\lambda} = \mathbf{F}_1\Delta\lambda + \begin{bmatrix}\mathbf{F}_{2F} & \mathbf{F}_{2B}\end{bmatrix}\begin{Bmatrix}\Delta\dot{\varepsilon}\\\Delta\beta\end{Bmatrix} + \begin{bmatrix}\mathbf{F}_{3F} & \mathbf{F}_{1B}\end{bmatrix}\begin{Bmatrix}\Delta\ddot{\varepsilon}\\\Delta\dot{\beta}\end{Bmatrix}. \tag{7}$$

Note that $(\cdot)|_0$ means a quantity evaluated at the given nonlinear equilibrium. With more details shown in the Appendix, Eq. (7) is used to form the state-space equation with control input and gust perturbation, given by

$$\dot{\mathbf{x}} = \mathbf{A}\mathbf{x} + \mathbf{B}\mathbf{u} + \mathbf{G}\mathbf{w}_g$$
$$\mathbf{y} = \mathbf{C}\mathbf{x} \tag{8}$$

where the state variable is

$$\mathbf{x}^T = \left\{ \Delta\varepsilon^T \quad \Delta\dot{\varepsilon}^T \quad \Delta\beta^T \quad \Delta\zeta^T \quad \Delta(\mathbf{p}_B^G)^T \quad \Delta\lambda^T \right\}. \tag{9}$$

Note that the output matrix ($\mathbf{C}$) is defined according to the individual problem.

2.4. Linear parameter-varying models

A significant challenge in the vibration control of highly flexible aircraft is that the wing deformation is inherently nonlinear under normal operating loads. The large wing deformation can further vary over time when the wing is also excited by a gust perturbation. Therefore, to achieve robust suppression against gust disturbances, the controller design of the gust alleviation of such aircraft cannot be based on a single or fixed equilibrium condition. Even though the gain-scheduling control can be used for new equilibrium conditions after some time intervals, based on which a new control input sequence can be calculated, the switching of the controller is usually not smooth, introducing additional vibration to the system.

The LPV approach [33] can be used for modeling and designing the vibration suppression controller. Ideally, the LPV model should be created based on the large wing deformation subject to the gust perturbation while the nominal flight velocity (or freestream velocity U_∞) is held constant. However, parameterizing the wing deformation is never trivial as it results from the vibration featuring an infinitive number of degrees of freedom. In this study, two approaches are considered to parameterize the wing deformation.

From the aerodynamic point of view, the gust velocity (in the vertical direction only, as considered in this study) alters the effective local angle of attack when applied along the wing span. Therefore, the first approach is to use the gust-induced angle of attack ($\alpha_g = \tan^{-1}(w_g/U_\infty)$) as the scheduling parameter to create the LPV models. For simplicity, this study only uses the α_g at the wing root as the single scheduling parameter, which can be justified by assuming a uniform gust. Under the nominal freestream velocity U_∞, the geometrical nonlinear wing deformations $\varepsilon(\alpha_g)$ can be solved with each prescribed α_g. Therefore, linearized models about each deformation $\varepsilon(\alpha_g)$ can be established that are parameter-dependent on α_g. Eventually, the LPV model can be created by interpolating the linearized models with the varying α_g. The discrete-time LPV reduced-order model (ROM) takes the form of

$$\mathbf{x}(k+1) = \mathbf{A}_d(\alpha_g(k))\mathbf{x}(k) + \mathbf{B}_d(\alpha_g(k))\mathbf{u}(k) + \mathbf{G}_d(\alpha_g(k))\mathbf{w}_g(k)$$
$$\mathbf{y}(k) = \mathbf{C}_d(\alpha_g(k))\mathbf{x}(k), \tag{10}$$

where the system matrices $\mathbf{A}_d(\alpha_g), \mathbf{B}_d(\alpha_g), \mathbf{G}_d(\alpha_g), \mathbf{C}_d(\alpha_g)$ are polynomially dependent on α_g. For instance, $\mathbf{A}_d(\alpha_g) = A_0 + A_1\alpha_g + A_2\alpha_g^2 + \cdots + A_p\alpha_g^p$. p denotes the order of polynomial. The discrete-time matrices are derived based on the zero-order hold method of states and scheduling parameter from the continuous-time system matrices.

The control design approach is essentially based on the awareness of external perturbation. It does involve the possible large wing deformation caused by the gust perturbation. However, such deformation is merely based on a simplified steady-state solution, excluding transient wing behavior. In addition, one will need to include more parameters (i.e., more measurements of gust-induced angle of attack along the wing span) to consider the spatial distribution of gust perturbation along the wing span, which complicates the construction of LPV models.

A second approach of parameterizing the wing deformation is based on the modal magnitudes of linear modes [33]. First, a modal reduction approach [49] is taken here, where the reference wing deformation is approximated by the combination of linear normal modes, given by

$$\varepsilon = \sum_j^\infty \boldsymbol{\Phi}_j\eta_j \tag{11}$$

where $\boldsymbol{\Phi}$ is the vehicle's linear normal strain mode matrix, and η is the corresponding magnitude of the modes. To obtain the normal modes in strain, one may use the first two entries of Eq. (7) and perform an eigenvalue analysis with the linearized stiffness and inertia matrices. As the stiffness matrix in Eq. (7) is singular, one can find six zero eigenvalues corresponding to the free-free rigid-body modes. The remaining eigenvalues correspond to the coupled elastic and rigid-body modes. The eigenvectors of these coupled modes generally take the form of

$$\boldsymbol{\Phi}_{\text{full}} = \begin{Bmatrix}\boldsymbol{\Phi}_F\\\boldsymbol{\Phi}_B\end{Bmatrix} \tag{12}$$

where $\boldsymbol{\Phi}_F$ and $\boldsymbol{\Phi}_B$ denote the elastic and rigid-body components of a mode, respectively. Since the modal approximation in Eq. (11) only
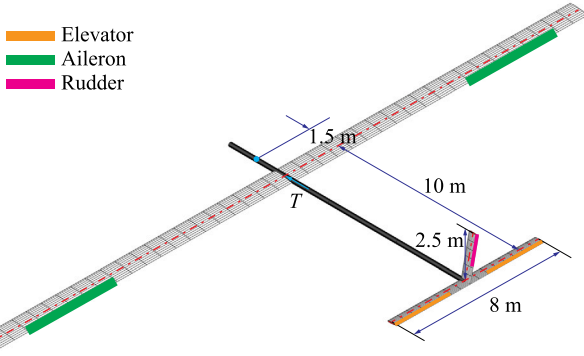
Fig. 3. Platform of flexible vehicle. (For interpretation of the colors in the figure(s), the reader is referred to the web version of this article.)

Fig. 4. Root loci of reduced-order LPV models of slender wing at different gust-induced angle of attack.

requires the elastic deformation, the rigid-body components of these modes are removed, i.e., $\boldsymbol{\Phi} = \boldsymbol{\Phi}_F$.

Nonetheless, once the modal magnitudes $\boldsymbol{\eta}_j$ are obtained, one can scale one dominant mode (represented by η) to get different wing deformations $\varepsilon(\eta)$ corresponding to the possibles that can be excited by an external gust. The next step is to linearize the equation of motion based on the wing deformations obtained from the scaled modal magnitudes $\varepsilon(\eta)$. Therefore, linearized models (7) at different deformation ε can be represented by the η-dependent system matrices. After that, the LPV model can be easily obtained by interpolating the linearized models at varying magnitude vectors. With the modal magnitude as the scheduling parameter, the discrete-time LPV model takes the form

$$\mathbf{x}(k+1) = \mathbf{A}_d(\eta(k))\mathbf{x}(k) + \mathbf{B}_d(\eta(k))\mathbf{u}(k) + \mathbf{G}_d(\eta(k))\mathbf{w}_g(k)$$
$$\mathbf{y}(k) = \mathbf{C}_d(\eta(k))\mathbf{x}(k), \tag{13}$$

where the system matrices $\mathbf{A}_d(\eta), \mathbf{B}_d(\eta), \mathbf{G}_d(\eta), \mathbf{C}_d(\eta)$ are polynomially dependent on η. For instance, the magnitude of the first mode η is considered a one-dimensional scheduling parameter to parameterize the wing deformation. Therefore, $\mathbf{A}_d(\eta) = A_0 + A_1\eta + A_2\eta^2 + \cdots + A_p\eta^p$. p denotes the order of the polynomial, which can be increased to obtain better interpolation accuracy.

This approach is essentially based on the awareness of possible wing deformation due to external excitation. It also involves the possible large wing deformation caused by the gust perturbation and excludes transient wing behavior. Nonetheless, it is possible to represent an accurate wing deformation by considering sufficient modes. In practice, the first symmetric and anti-symmetric modes can be included to reasonably approximate the wing deformation due to a spatially-distributed gust. As the wing deformation can be assumed as a weighted summation of selected linear modes, it excludes the possible impact of unmodeled modes. Moreover, the mode shapes of the slender wings are calculated about the reference deformation, which may change with the wing deformation.

In summary, the LPV modeling procedure mainly consists of four steps: 1) Grid flexible wing into a finite number of beam elements and derive nonlinear dynamic Eq. (2); 2) Linearize the nonlinear model and transform to modal coordinate at a series of grid scheduling parameter (α_g, η) to obtain LTI modal full-order models; 3) Align the modes to capture the evolution at varying scheduling parameter for model-reduction by keeping the most significant modes; and 4) Interpolate to a polynomial parameter-dependent LPV-ROM, and conduct discrete-time conversion by zero-order hold method. More details of LPV modeling procedures can be found in [50,33].

2.5. Model predictive control with LPV model

In this paper, the control objective is to alleviate the gust disturbance by model predictive control based on the LPV models (13) while stabilizing rigid-body motions around the equilibrium point. With the
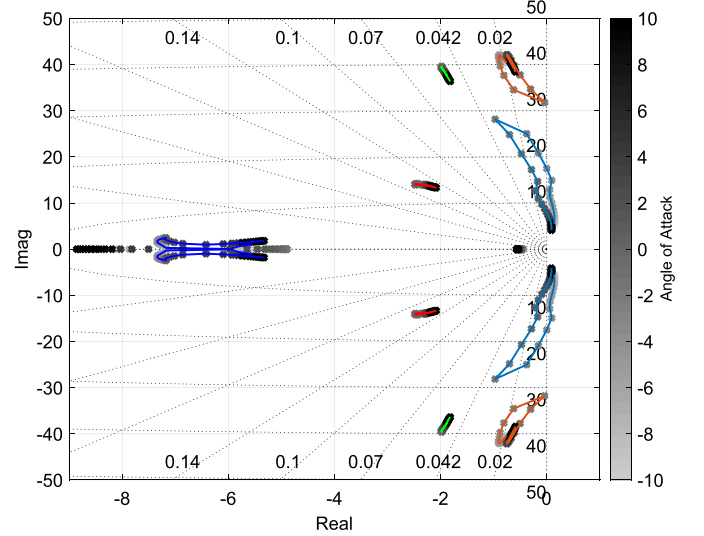
commercial radar/Lidar sensors [45], the gust perturbation w_g ahead of the aircraft is assumed to be detected in a finite prediction horizon. Therefore, the scheduling parameter (α_g or η) can be previewed/calculated in the prediction horizon, and the LPV model will be converted to a sequence of linear time-varying (LTV) models in the prediction horizon. Note that the domain of the scheduling parameter of LPV models should cover the possible flight conditions of concern.

For the sake of simplicity, θ is used to denote the scheduling parameter α_g and η, i.e. $\theta = \{\alpha_g, \eta\}$, and its domain is written as $\theta \in \Theta$. At each time step, with the given/previewed N-lengthy sequences of gust sequence $\mathbf{w}_g$ and scheduling parameter $[\theta(0), \theta(1), \cdots, \theta(N-1)]$, the control sequence $\mathbf{U} = [\mathbf{u}(0), \mathbf{u}(1), \cdots, \mathbf{u}(N-1)]$ are obtained by solving the following optimization problem:

$$\min_{\mathbf{U}} \mathbf{y}^T(N)\boldsymbol{Q}_f\mathbf{y}(N) + \sum_{k=0}^{N-1}\left(\mathbf{y}^T(k)\boldsymbol{Q}\mathbf{y}(k) + \mathbf{u}^T(k)\boldsymbol{R}\mathbf{u}(k)\right)$$

s.t.
$$\mathbf{x}(k+1) = \mathbf{A}_d(\theta(k))\mathbf{x}(k) + \mathbf{B}_d(\theta(k))\mathbf{u}(k) + \mathbf{G}_d(\theta(k))\mathbf{w}_g(k)$$
$$\mathbf{y}(k+i) = \mathbf{C}_d(\theta(k))\mathbf{x}(k),$$
$$\theta \in \Theta, \mathbf{x}(k) \in \mathcal{X}, \tag{14}$$
input constraint :
$$\mathbf{u}(k) = \left[u_1(k), \ldots, u_m(k)\right]^T$$
$$\mathbf{u}_{\min} \leqslant \mathbf{u}(k) \leqslant \mathbf{u}_{\max},$$
$$\Delta\mathbf{u}_{\min} \leqslant \mathbf{u}(k+1) - \mathbf{u}(k) \leqslant \Delta\mathbf{u}_{\max},$$

Remark 1 (*stability and recursive feasibility*). To achieve the closed-loop stability and recursive feasibility of LPV-MPC, the terminal weighting matrix $\boldsymbol{Q}_f$ and positive invariant set $\mathcal{X}$ need to be calculated or checked to satisfy stability conditions. Parametric linear matrix inequalities (PLMIs) borrowed from [35,47] are used in this work to find terminal cost and set. More methods to calculate robust invariant set can also be found in [51] to achieve guaranteed robustness. The detailed proofs of stability and recursive feasibility are omitted here since they are established in [35,47]. The weighting matrices and invariant set of states are checked or calculated to satisfy the PLMIs, thus achieving stability and recursive feasibility. The stability is demonstrated in the numerical results by the fast convergence to a steady state after the gust disturbance disappears.
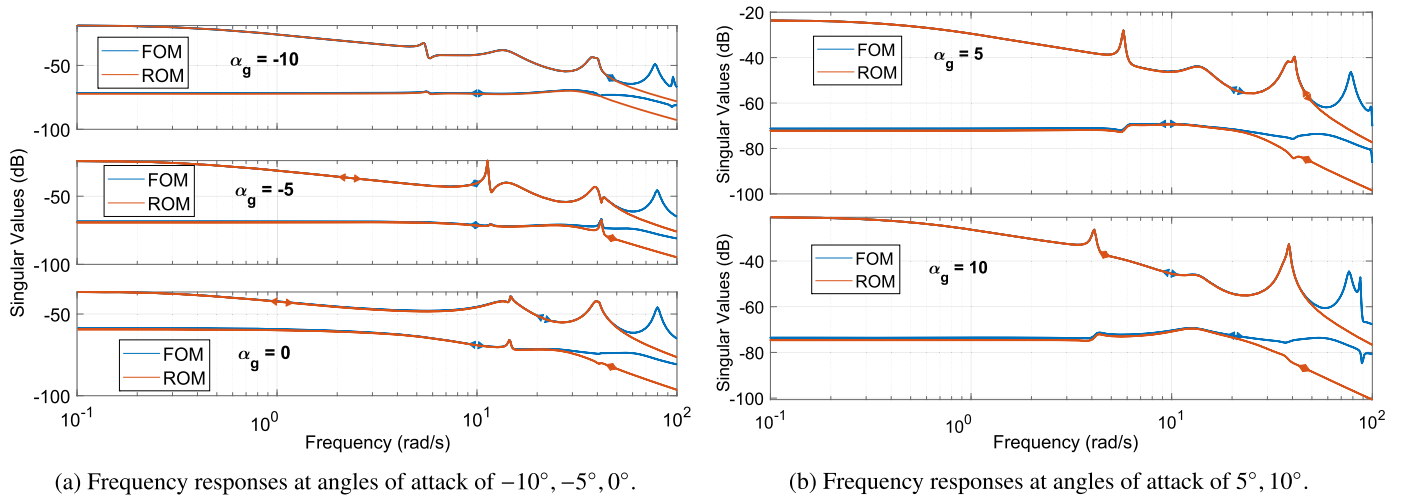
(a) Frequency responses at angles of attack of $-10°, -5°, 0°$.

(b) Frequency responses at angles of attack of $5°, 10°$.

Fig. 5. Frequency-domain responses comparisons of ROMs and FOMs at grid angles of attack.

(a) Gust disturbance with sampling frequency 10 Hz.
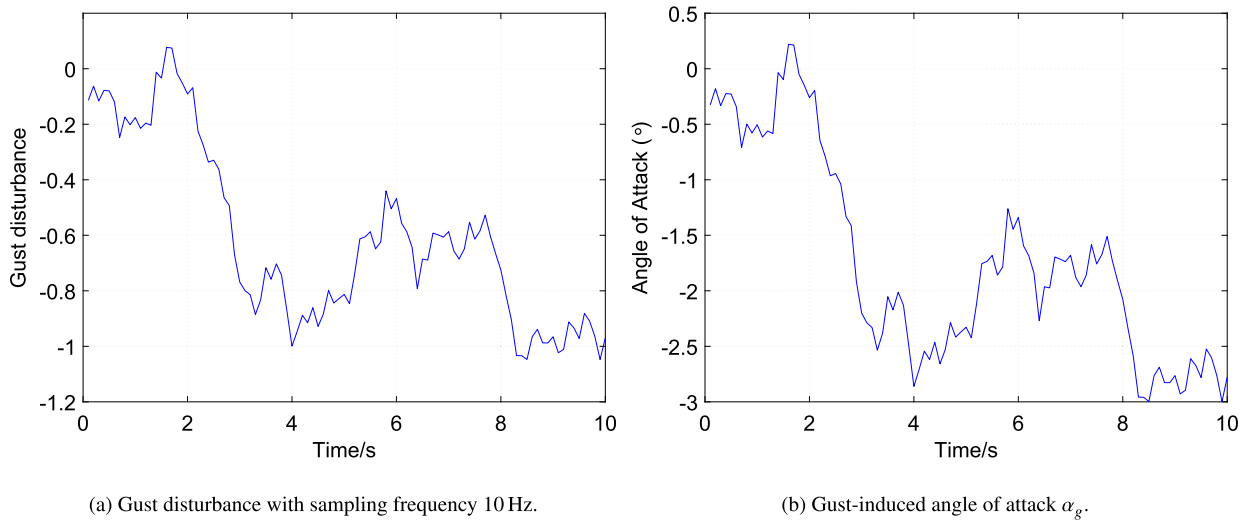
(b) Gust-induced angle of attack α_g.

Fig. 6. Sampled gust disturbance and corresponding gust-induced angle of attack.


(a) Control input (flap deflection angle) of LPV-MPC.

(b) Bending strains y_1 (wing root), y_5 (mid-span), and y_{10} (wing tip).
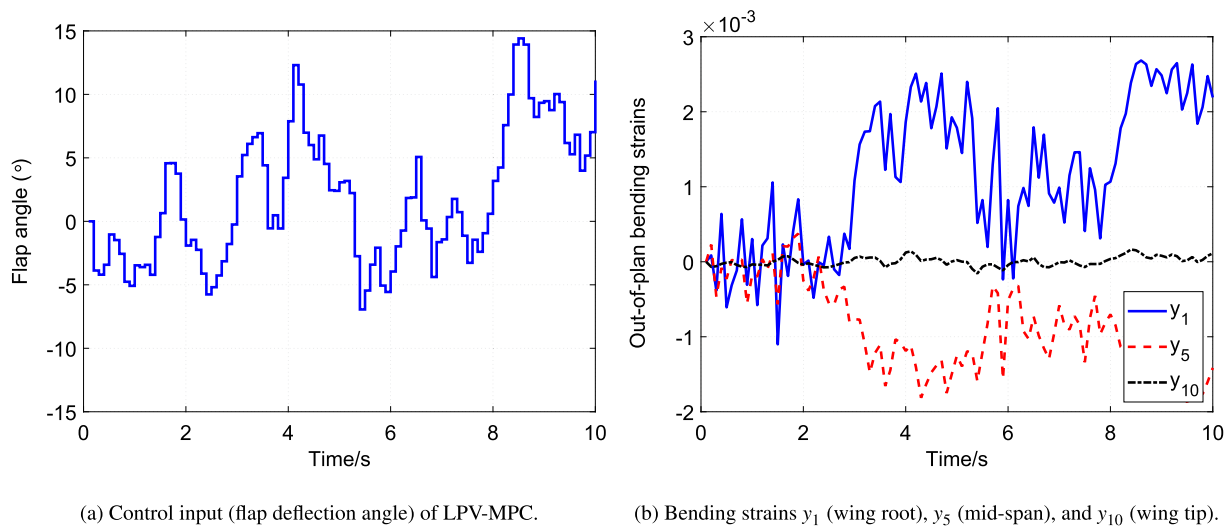
Fig. 7. Control input of flap deflection angles and strains output along the slender wing.
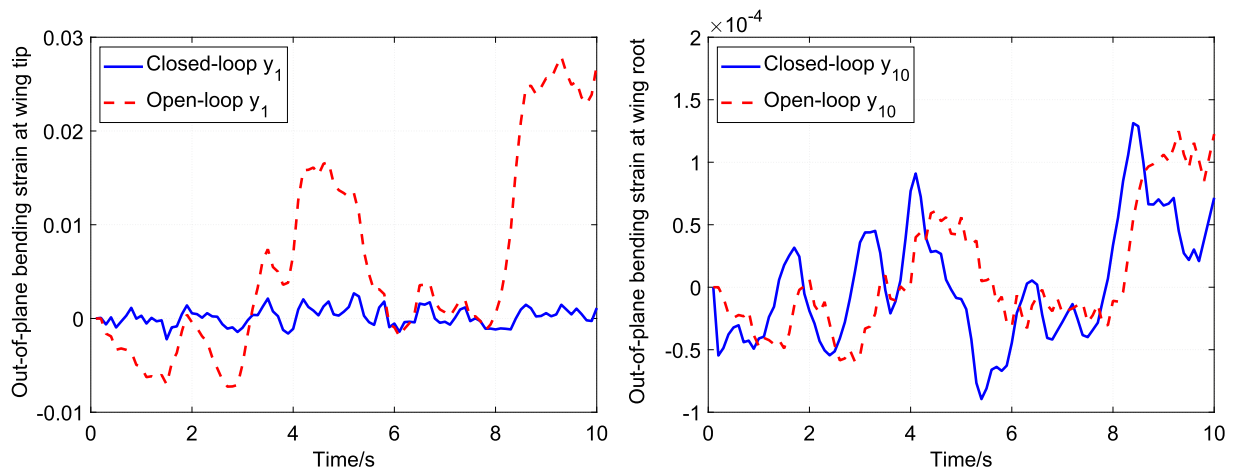
(a) Open-loop and closed-loop responses of y_1 at wing root.

(b) Open-loop and closed-loop responses of y_{10} at wing tip.

Fig. 8. Open-loop and closed-loop responses of bending strains on the slender wing.
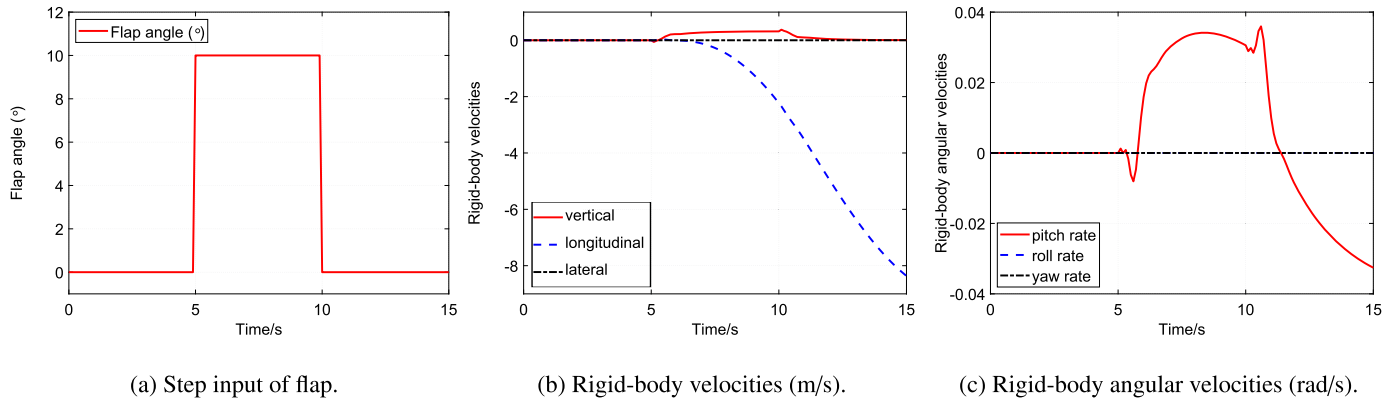
(a) Step input of flap.

(b) Rigid-body velocities (m/s).

(c) Rigid-body angular velocities (rad/s).

Fig. 9. Rigid-body velocities and angular velocities responding to the step input of flap.
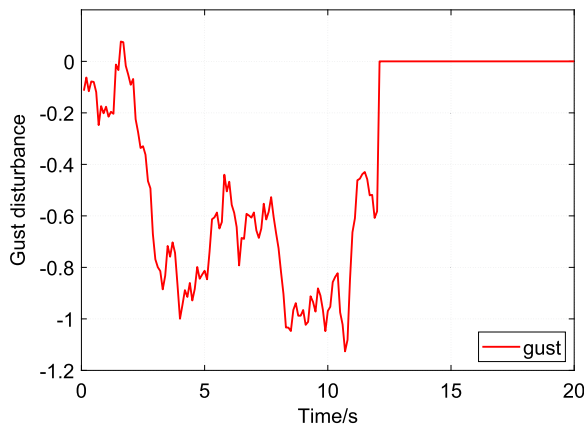
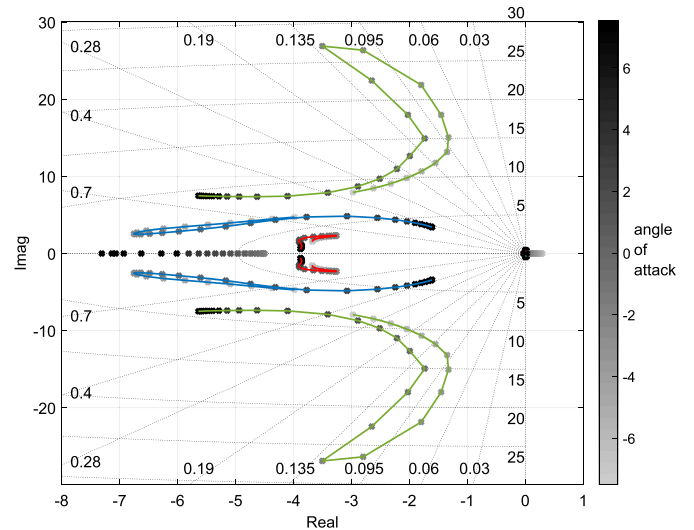

Fig. 10. Gust disturbance for highly flexible vehicle.

Fig. 11. Root loci of LPV-ROM of flexible vehicle at different gust-induced angles of attack.

3. Numerical studies

Several studies regarding the gust alleviation of highly flexible aircraft are performed using the LPV-MPC method and the results are reported in this section.

3.1. Highly flexible wing and aircraft models

As shown in Fig. 3, the highly flexible aircraft in this study is modified from the one provided in [4]. The physical and geometrical prop-
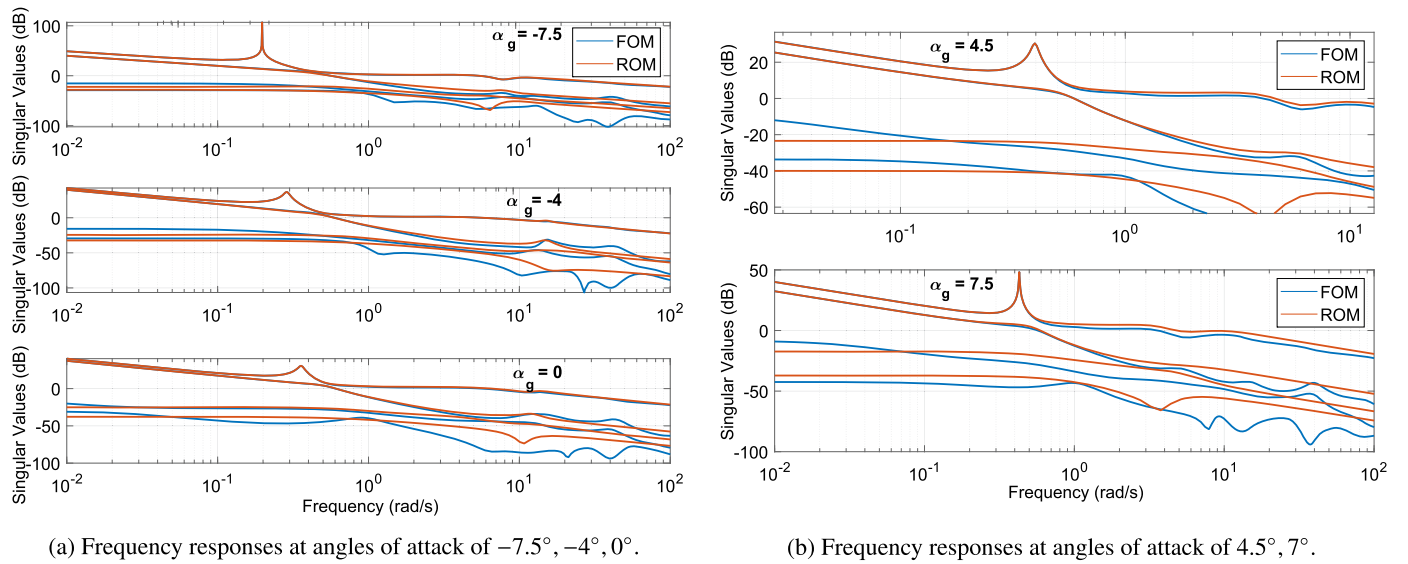
(a) Frequency responses at angles of attack of $-7.5°, -4°, 0°$.

(b) Frequency responses at angles of attack of $4.5°, 7°$.

Fig. 12. Frequency-domain responses comparisons of ROMs and FOMs at grid angles of attack.
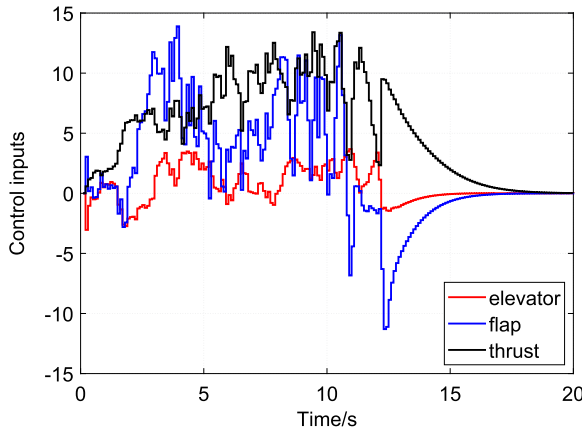

Fig. 13. Inputs of flap and elevator (unit in degree), and thrust (unit in N).

Table 1
Properties of a highly flexible wing.

Quantity	Value
Length	16 m
Chord	1 m
Spanwise ref. axis location (from L.E.)	50% of chord
Center of gravity (from L.E.)	50% of chord
Torsional rigidity	1×10^4 Nm^2
Flat bending rigidity	2×10^4 Nm^2
Chord bending rigidity	4×10^6 Nm^2
Mass per unit length	0.75 kg/m
Rotational Inertia per unit length	0.1 kgm

erties of the wing are given in Table 1. All members of the aircraft are modeled as slender beams. However, the body and tail members are 100 times stiffer than the main wing, although they all have the same inertial properties. The chord length of the horizontal and vertical tails is 0.5 m, while their beam reference lines are defined at a quarter of the chord from the leading edge. There is no aerodynamics coupled on the body. The main wing is divided into ten elements. Discrete trailing-edge control surfaces on the main wing are defined from its 60% to 90% span, occupying 20% of the chord. Similar surfaces are also defined on the horizontal tail, from its 25% to the full span. The flaps on the hor-

izontal tail are used as elevators to trim the vehicle for level flight. In addition, they are used together with the control surfaces on the main wing for gust vibration control.

3.2. Gust alleviation of highly flexible wing

The flexible cantilever wing is placed in a freestream of $U_\infty = 20$ m/s at 20,000 m altitude. The outputs of concern are the out-of-plane bending strains $\Delta\varepsilon$ on each beam element, from wing root y_1 to wing tip y_{10}. The control authority used in the vibration control is the flap deflection angle.

The LPV-ROM is developed first to carry out the controller design and simulation for gust alleviation of such a highly flexible wing. The full-order nonlinear aeroelastic system is linearized at grid points of the gust-induced angle of attack $\alpha_g \in [-10°, 10°]$ with an increment of 0.5°, leading to a series of full-order linearized aeroelastic models (FOM). Next, modal cost analysis is performed to obtain the reduced-order LTI models by keeping the most significant modes. The dimension of the resulting ROM is 12, and the root loci of the ROM are shown in Fig. 4. An LPV model can then be interpolated into a 4th-order polynomial LPV model. The frequency-domain comparisons between FOM and LPV-ROM at grid points of the angle of attack are shown in Fig. 5. It is shown that the LPV-ROM captures the dominant dynamic behaviors in the frequency range of 0.1–50 rad/s.

The continuous gust disturbance is sampled at 10 Hz, as shown in Fig. 6a, which is uniformly applied on the flexible wing to excite its vibration. The LPV-MPC is then designed and applied to suppress the wing vibration. The scheduling parameter, gust-induced angle of attack, is plotted in Fig. 6b. The weighting matrices and parameters of the LPV-MPC are selected as follows: the prediction horizon length $N = 20$, total simulation time steps $N_t = 100$, sampling time $T_s = 0.1$ s, $Q = Q_f = 10^5 I_{10}$, and $R = 1$, where Q_f is the weighting of terminal tracking error, and Q is the weighting of prediction-horizon tracking error. The constraints of control inputs are enabled as $\mathbf{u}_{max} = 20°$, $\mathbf{u}_{min} = -20°$, $\Delta\mathbf{u}_{max} = 5°$, $\Delta\mathbf{u}_{min} = -5°$.

The control input and wing bending strain outputs are shown in Fig. 7. Fig. 8 shows the comparisons between the open-loop and controlled responses of the out-of-plane bending strain at the wing root y_1 and wing tip y_{10}, respectively. It can be seen that the LPV-MPC can effectively suppress the gust-induced vibration. The l_2 norm (energy) of un-controlled strains responses are reduced by 91.7% to controlled responses of y_1 at the wing root, and reduced by 6.28% of y_{10} at the wing
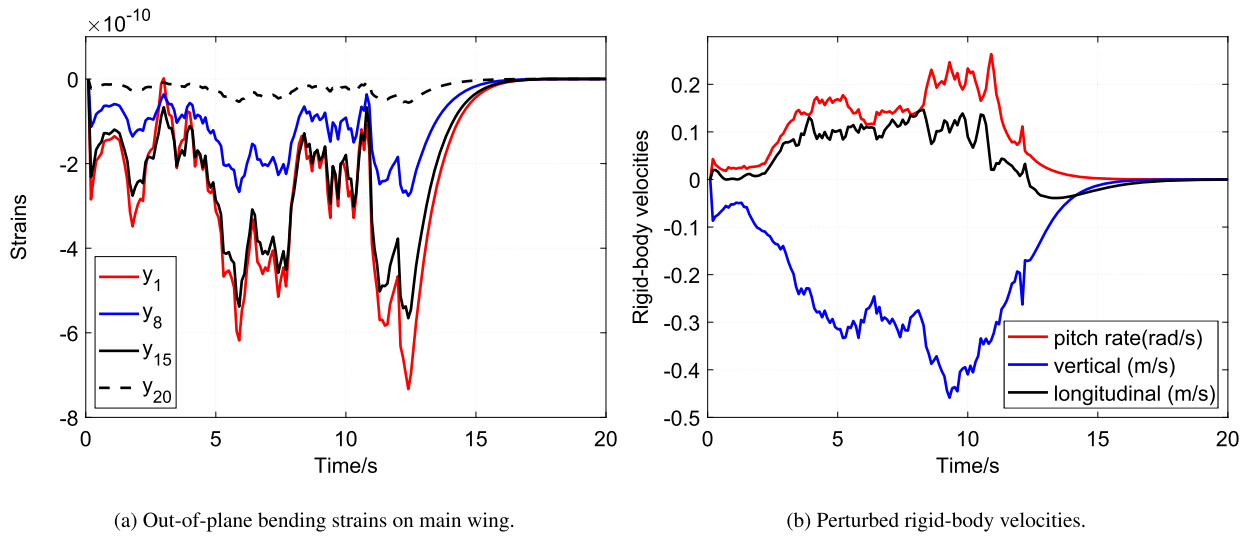
(a) Out-of-plane bending strains on main wing.

(b) Perturbed rigid-body velocities.

Fig. 14. Closed-loop responses of bending strains and rigid-body velocities under LPV-MPC, with y_1 at wing root and y_{20} at wing tip.
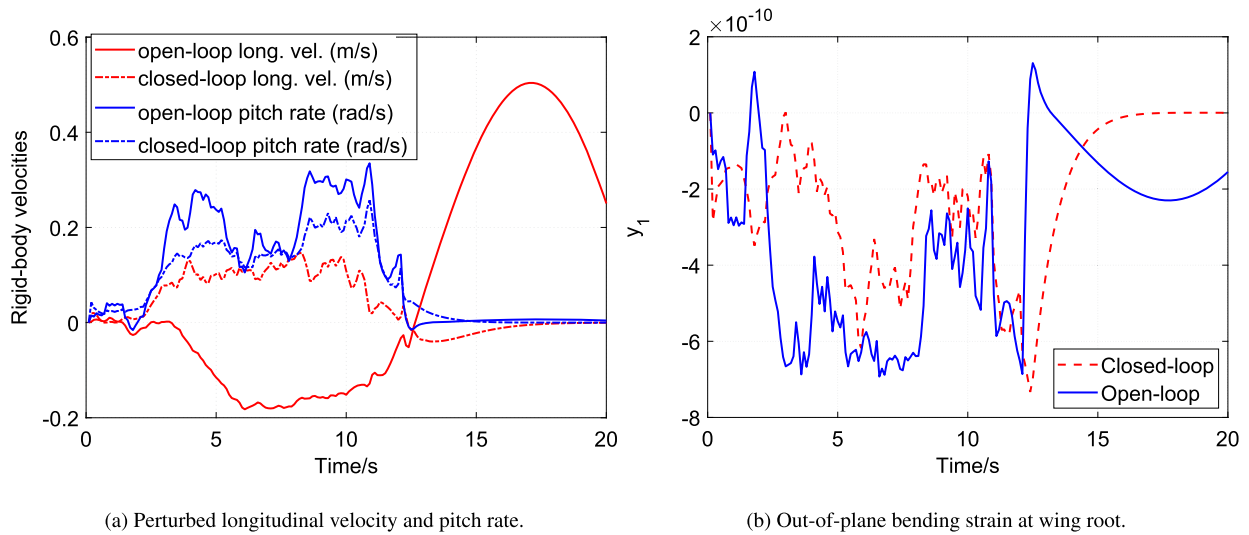

(a) Perturbed longitudinal velocity and pitch rate.

(b) Out-of-plane bending strain at wing root.

Fig. 15. Comparisons of the closed-loop and open-loop responses.
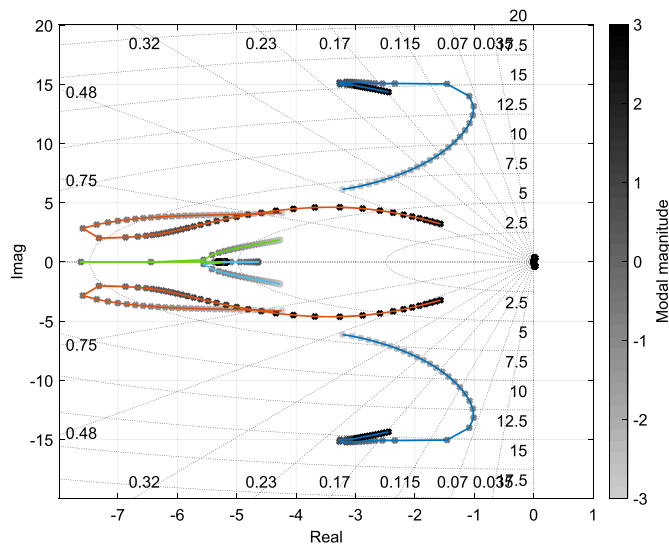
Fig. 16. Root loci of reduced-order LPV model of flexible vehicle at different modal magnitudes.

tip. The reductions of l_2 norms of all bending strains on the main wing are 82.9%.

3.3. Gust alleviation of highly flexible aircraft

The vibration suppression coupled with rigid-body motion control of the highly flexible aircraft is also investigated using the LPV-MPC approach. The coupled aeroelastic and flight dynamic components are included in the FOMs. The control input of the flap angle suppressing the vibrations will impact the rigid-body motions because of the coupled dynamics. The open-loop responses by a step input of flap angle are plotted in Fig. 9, demonstrating the coupled dynamics and the necessity of including the rigid-body dynamics in the model.

The following control scenario is studied. The aircraft is cruising at the velocity of $U_\infty = 22$ m/s at 20,000 m altitude. It is subject to the gust disturbance shown in Fig. 10, which is symmetric and uniformly applied on both the wing and tail. The gust is turned off after 12 s. The control inputs are flaps on the main wing, elevator on the tail, and thrust. The outputs of interest are out-of-plane bending strains of the main wings, body longitudinal velocity, vertical velocity, pitch angular velocity, body pitch angle, longitudinal position, and vertical position.
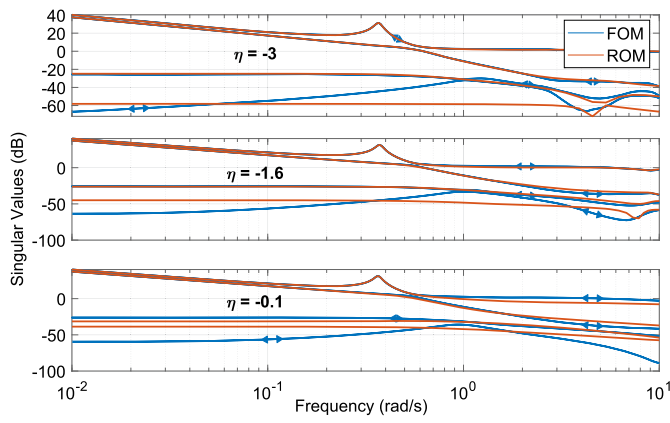
(a) Frequency-domain comparisons between FOM and LPV-ROM at modal magnitude $\eta = -3, -1.6, -0.1$.
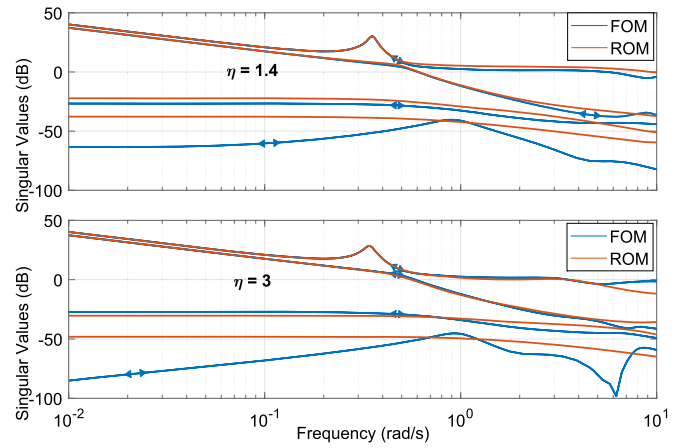
(b) Frequency-domain comparisons between FOM and LPV-ROM at modal magnitude $\eta = 1.4, 3$.

Fig. 17. Frequency responses comparisons of FOM and LPV-ROM at grid points of modal magnitude.
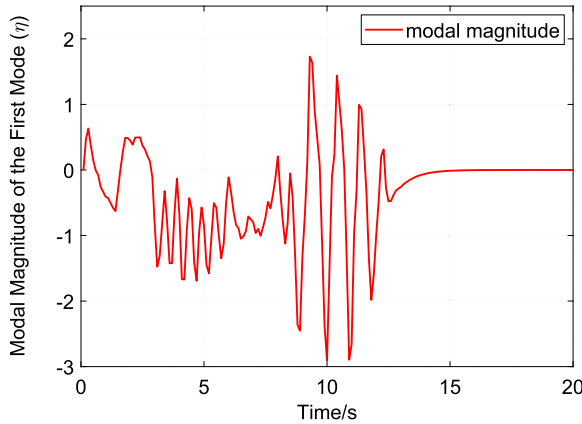

Fig. 18. Modal magnitude of the first mode (scheduling parameter) of flexible vehicle.

3.3.1. Gust-induced angle of attack as scheduling parameter

Firstly, the reduced-order LPV model is derived, considering the gust-induced angle of attack within the range of $\alpha_g \in [-7.5°, 7.5°]$ with an increment of 0.5°. The root loci of the reduced-order model are shown in Fig. 11. The order of the reduced-order model is 12. Interestingly, the root loci differ from the cantilever wing because the rigid-body modes are considered in the full flexible vehicle study. The contributions of the modes are changed relative to rigid-body motion.

The reduced-order models are validated and compared with the full-order system in the time and frequency domains. The frequency domain responses at grid angles of attacks are plotted in Fig. 12. It is demonstrated that the LPV-ROM matches with the FOMs at grid points of the angle of attack, and the LPV-ROM can capture the parameter-dependent coupled modes of rigid-body and aeroelasticity.

The particular challenges in the LPV-MPC are two-fold. First, the dynamic model is time-varying and is parameter-dependent on the angle of attack induced by the gust disturbance. In addition, the rigid-body dynamics shall be regulated simultaneously with the wing vibration suppression because the input of the flap can excite the rigid-body motion. The LPV-MPC updates the models in the prediction horizon and optimizes the control inputs (flap, elevator, and thrust) to stabilize the rigid-body motions and suppress the wing vibration.

The LPV-MPC is then designed and simulated with the same scheduling parameter (gust-induced angle of attack). The weighting matrices are selected as $Q = Q_f = diag(10^8 I_{20}, 10^2 I_6)$ and $R = I_3$. The constraints

of control are specified as $|u_{flap}| \leqslant 20°$, $|u_{elevator}| \leqslant 20°$, $0 \leqslant u_{thrust} \leqslant 50$ N, $|\Delta u_{flap}| \leqslant 5°$, and $|\Delta u_{elevator}| \leqslant 5°$.

The time-domain simulation results are shown in Figs. 13 and 14. In the presence of gust disturbance from 0 to 12 s, the LPV-MPC can successfully suppress the vibrations on the main wing and maintain perturbed rigid-body motions at very small levels simultaneously. When the gust disturbance disappears at the end of 12 s, the LPV-MPC can rapidly bring the vibrations and perturbed rigid-body motions to a steady state. Furthermore, it can be seen that the wing deformation (strain) is significantly smaller compared to the cantilever slender wing case. The reason is that only one control input of the flap was used for the vibration control of the cantilever wing. However, the flexible vehicle has control authority of the main wing flap and the elevator on the tail. More degrees of freedom of control provide a much better vibration suppression on the wing. In other words, the control inputs of thrust and elevator deflection can also contribute to vibration suppression, which matches the physical sense.

The corresponding comparisons of the open-loop and closed-loop responses of rigid-body velocities and bending strain at wing root (y_1) are shown in Fig. 15. First, the open-loop responses of longitudinal velocity and strain at the wing root present large oscillation when the gust disturbance disappears at 12 s. However, the LPV-MPC can achieve a rapid convergence to zero. Besides, the vibrations are suppressed by the LPV-MPC with a reduction ratio of 86.3%, compared to the open-loop vibrations responses.

3.3.2. Modal magnitude as scheduling parameter

The approach using the modal magnitude as the LPV scheduling parameter is then investigated to derive the LPV-ROM and design the LPV-MPC to suppress the wing vibration and stabilize the rigid-body motions. The root loci of the derived reduced-order LPV model are shown in Fig. 16, where the modal magnitude ranges in $[-3, 3]$ with an increment of 0.1. The reduced-order model has the order of 10. In Fig. 17, the frequency responses of the FOM and LPV-ROM are compared at grid points of modal magnitudes, which demonstrate the accuracy of the LPV-ROM across the range of scheduling parameter.

Note that since the modal magnitude η is the scheduling parameter, the predicted magnitude of the first wing bending mode is used to interpolate and determine the models in the prediction horizon, which is plotted in Fig. 18. In practice, the modal magnitude can generally be derived based on the measurement of strain gauges distributed along the wing. The cost functions, weighting functions, and constraints on control inputs are the same as in the previous study.
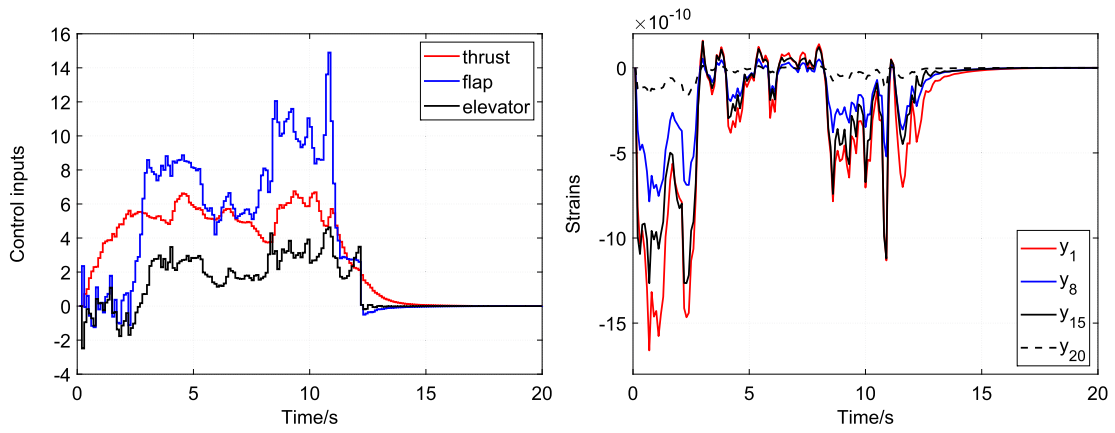
(a) Control inputs of flap, elevator (unit: degree) and thrust (unit in N) by LPV-MPC in modal magnitude approach.

(b) Strain outputs on the main wing by LPV-MPC, with y_1 at wing root and y_{20} at wing tip.
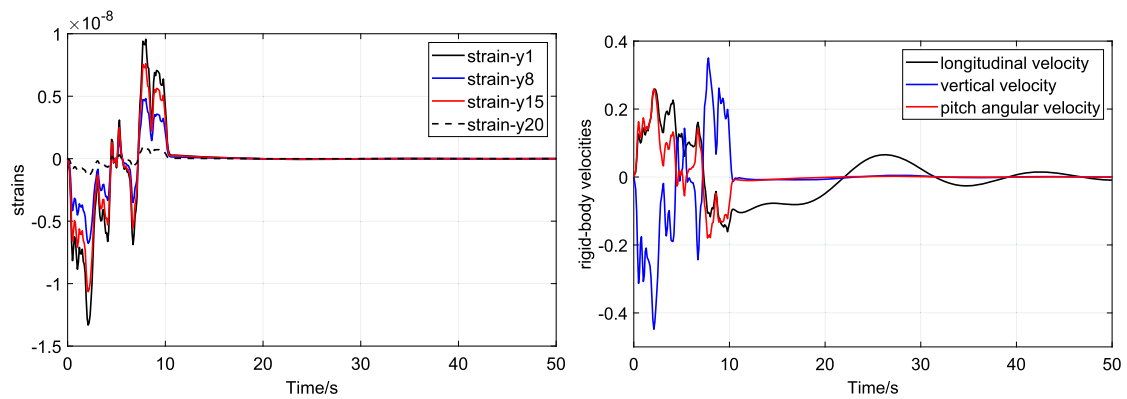
Fig. 19. Strains and control inputs by LPV-MPC.
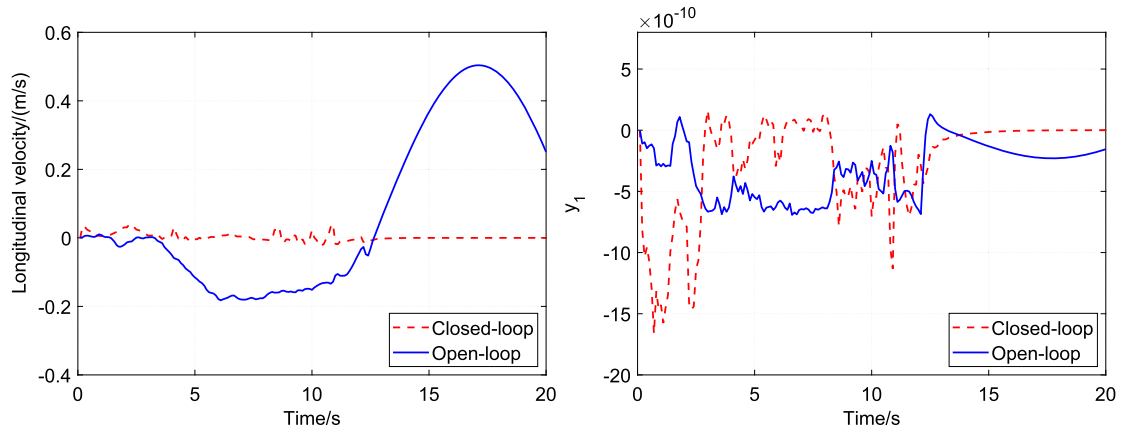
(a) Perturbed longitudinal velocity.

(b) Out-of-plane bending strain at wing root.

Fig. 20. Comparisons of the closed-loop and open-loop responses.

(a) Out-of-plane bending strains.

(b) Perturbed rigid-body velocities.

Fig. 21. Closed-loop responses of bending strains and rigid-body velocities by LQG control.
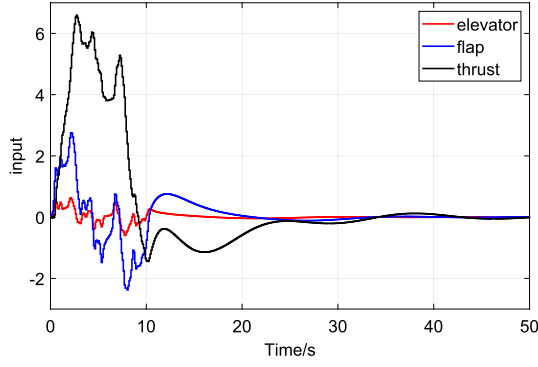
Fig. 22. Control inputs by LQG controller.

The time-domain simulation results are obtained by employing the LPV-MPC. The control inputs of the LPV-MPC are plotted in Fig. 19a, and the corresponding strains outputs are plotted in Fig. 19b. For comparisons between open-loop and closed-loop responses, the longitudinal velocity is plotted in Fig. 20a, and the out-of-plane bending strain at wing root y_1 is shown in Fig. 20b. The LPV-MPC designed based on the LPV-ROM can suppress the wing vibrations on the span and limit the rigid-body motions against the gust disturbance. The gust is also turned off at 12 s. The LPV-MPC can regulate the bending strains and rigid-body velocities to zero. These time-domain responses demonstrate the performance and robustness of the designed LPV-MPC using the modal magnitude as the scheduling parameter. The LPV-MPC can achieve 53.7% reduction from open-loop responses from the open-loop responses, while maintaining the rigid-body motions within small perturbations of 0.5 m/s.

The comparison against a baseline LQG controller is conducted to illustrate the excellent performance of the LPV-MPC using modal magnitude. The LQG controller is designed based on a linear reduced-order model at fixed modal magnitude $\eta = 0$, often used in traditional control methods for small wing deformation. For a fair comparison, the LQG weighting matrices $\boldsymbol{Q}$, $\boldsymbol{R}$ are selected same as LPV-MPC. The time-domain simulation results by LQG control are presented in Figs. 21 and 22. Although the LQG control can also stabilize vibrations and rigid-body perturbations, it performs worse than LPV-MPC. First, in the presence of gust disturbance, the LQG controller renders larger magnitudes of strains on the wing and rigid-body motions. Second, after gust disturbance disappears, the LQG controller takes much longer to regulate the perturbed rigid-body motions than LPV-MPC. The reason is that the LQG controller only uses the small-deformation model rather than the parametric models at varying modal magnitudes and previewing gust disturbance, which are adopted in the LPV-MPC.

The robustness of LPV-MPC is further investigated against model uncertainty. The modal magnitude of the first mode is perturbed with an additive uncertainty of 10%, and the simulation results are plotted in Figs. 23 and 24. It can be seen that the LPV-MPC can still stabilize the rigid-body velocities and suppress the bending strains at low levels. The magnitudes of the strains and rigid-body motions are slightly worse than the results without additive uncertainty. This numerical study illustrates the robustness capability and further theoretical analysis and control algorithm development on the robustness capability of LPV-MPC is future work.

4. Conclusion

This paper explored the development of methodologies that allow for robust vibration control for highly flexible wings and aircraft. While the coupled nonlinear aeroelasticity and flight dynamic behavior of highly flexible aircraft was governed by a set of nonlinear equations, the current method utilized the linearized aeroelastic systems that vary based on selected scheduling parameters, relevant to the gust pertur-

bation and/or the resulting wing vibration. The model predictive controller was then designed based on the LPV models for aircraft vibration control. This study considered two scheduling parameters: the gust-induced angle of attack and the linear modes' modal magnitude. The current study also focused on simplified cases where the gust perturbation was uniformly applied everywhere on the vehicle or the wing, allowing one to use either the gust-induced angle of attack at the wing root or the magnitude of the first symmetric bending mode as the scheduling parameter. More complicated cases can be considered by expanding the scheduling parameters. The developed controllers were then applied to the linearized models for the time simulation. The simulation results showed that the controller designed using the modal magnitude performed better in gust suppression.

Declaration of competing interest

The authors declare that they have no known competing financial interests or personal relationships that could have appeared to influence the work reported in this paper.

Data availability

Data will be made available on request.

Appendix A. Additional equations for state-space formulation

In Eq. (7), the linearized inertia, damping, and stiffness matrices are

$$
\bar{\mathbf{M}}_{FF} = \mathbf{M}_{FF_0} - \frac{\partial \mathbf{R}_F^{\text{aero}}}{\partial \ddot{\varepsilon}}\bigg|_0, \qquad \bar{\mathbf{M}}_{FB} = \mathbf{M}_{FB_0} - \frac{\partial \mathbf{R}_F^{\text{aero}}}{\partial \dot{\boldsymbol{\beta}}}\bigg|_0,
$$
$$
\bar{\mathbf{M}}_{BF} = \mathbf{M}_{BF_0} - \frac{\partial \mathbf{R}_B^{\text{aero}}}{\partial \ddot{\varepsilon}}\bigg|_0, \qquad \bar{\mathbf{M}}_{BB} = \mathbf{M}_{BB_0} - \frac{\partial \mathbf{R}_B^{\text{aero}}}{\partial \dot{\boldsymbol{\beta}}}\bigg|_0,
$$
(A.1)

$$
\bar{\mathbf{C}}_{FF} = - \frac{\partial \mathbf{R}_F^{\text{damp}}}{\partial \dot{\varepsilon}}\bigg|_0 - \frac{\partial \mathbf{R}_F^{\text{aero}}}{\partial \dot{\varepsilon}}\bigg|_0, \qquad \bar{\mathbf{C}}_{FB} = - \frac{\partial \mathbf{R}_F^{\text{damp}}}{\partial \boldsymbol{\beta}}\bigg|_0 - \frac{\partial \mathbf{R}_F^{\text{aero}}}{\partial \boldsymbol{\beta}}\bigg|_0,
$$
$$
\bar{\mathbf{C}}_{BF} = - \frac{\partial \mathbf{R}_B^{\text{damp}}}{\partial \dot{\varepsilon}}\bigg|_0 - \frac{\partial \mathbf{R}_B^{\text{aero}}}{\partial \dot{\varepsilon}}\bigg|_0, \qquad \bar{\mathbf{C}}_{BB} = - \frac{\partial \mathbf{R}_B^{\text{damp}}}{\partial \boldsymbol{\beta}}\bigg|_0 - \frac{\partial \mathbf{R}_B^{\text{aero}}}{\partial \boldsymbol{\beta}}\bigg|_0,
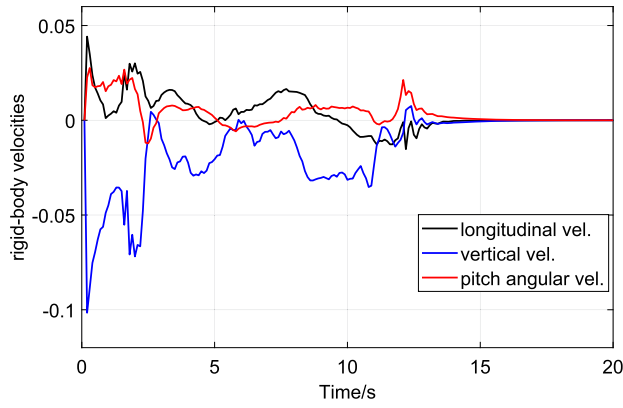$$
(A.2)

and

$$
\bar{\mathbf{K}}_{FF} = \mathbf{K}_{FF_0} - \frac{\partial \mathbf{R}_F^{\text{aero}}}{\partial \varepsilon}\bigg|_0, \qquad \bar{\mathbf{K}}_{BF} = - \frac{\partial \mathbf{R}_B^{\text{aero}}}{\partial \varepsilon}\bigg|_0,
$$
(A.3)
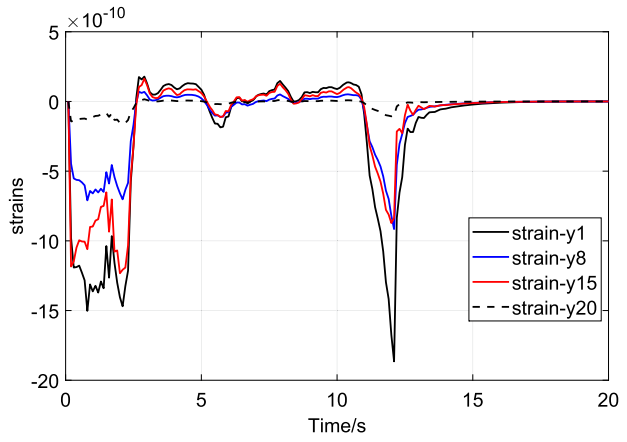
respectively. Eq. (7) is further written in the state-space form, given by

$$
\dot{\mathbf{x}} = \mathbf{Q}_1^{-1}\mathbf{Q}_2\mathbf{x} + \mathbf{Q}_1^{-1}\mathbf{Q}_3\mathbf{u} + \mathbf{Q}_1^{-1}\mathbf{Q}_4\mathbf{w}_g
$$
$$
= \mathbf{A}\mathbf{x} + \mathbf{B}\mathbf{u} + \mathbf{G}\mathbf{w}_g
$$
(A.4)

where

$$
\mathbf{Q}_1 = \begin{bmatrix} \mathbf{I} & \mathbf{0} & \mathbf{0} & \mathbf{0} & \mathbf{0} & \mathbf{0} \\ \mathbf{0} & \bar{\mathbf{M}}_{FF} & \bar{\mathbf{M}}_{FB} & \mathbf{0} & \mathbf{0} & \mathbf{0} \\ \mathbf{0} & \bar{\mathbf{M}}_{BF} & \bar{\mathbf{M}}_{BB} & \mathbf{0} & \mathbf{0} & \mathbf{0} \\ \mathbf{0} & \mathbf{0} & \mathbf{0} & \mathbf{I} & \mathbf{0} & \mathbf{0} \\ \mathbf{0} & \mathbf{0} & \mathbf{0} & \mathbf{0} & \mathbf{I} & \mathbf{0} \\ \mathbf{0} & -\mathbf{F}_{3F} & -\mathbf{F}_{3B} & \mathbf{0} & \mathbf{0} & \mathbf{I} \end{bmatrix}
$$
(A.5)

(a) Closed-loop responses of Rigid-body velocities under model uncertainty.

(b) Closed-loop responses of strains under model uncertainty.

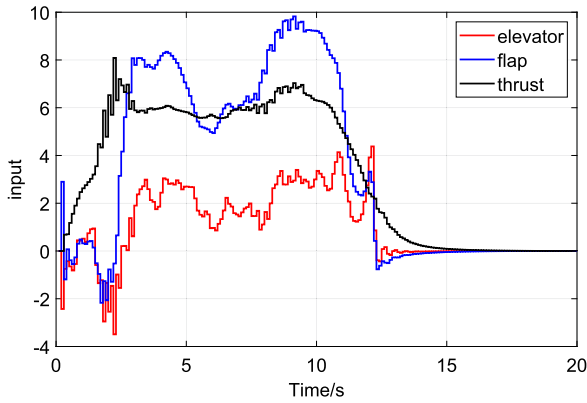**Fig. 23.** Closed-loop responses of LPV-MPC under model uncertainty.

Fig. 24. Control inputs of LPV-MPC against model uncertainty.

$$\mathbf{Q}_2 = \begin{bmatrix} \mathbf{0} & \mathbf{I} & \mathbf{0} & \mathbf{0} & \mathbf{0} & \mathbf{0} \\ -\bar{\mathbf{K}}_{FF} & -\bar{\mathbf{C}}_{FF} & -\bar{\mathbf{C}}_{FB} & \left.\dfrac{\partial \mathbf{R}_F^{\mathrm{grav}}}{\partial \zeta}\right|_0 & \mathbf{0} & \left.\dfrac{\partial \mathbf{R}_F^{\mathrm{aero}}}{\partial \lambda}\right|_0 \\ -\bar{\mathbf{K}}_{BF} & -\bar{\mathbf{C}}_{BF} & -\bar{\mathbf{C}}_{BB} & \left.\dfrac{\partial \mathbf{R}_B^{\mathrm{grav}}}{\partial \zeta}\right|_0 & \mathbf{0} & \left.\dfrac{\partial \mathbf{R}_B^{\mathrm{aero}}}{\partial \lambda}\right|_0 \\ \mathbf{0} & \mathbf{0} & -\dfrac{1}{2}\left.\dfrac{\partial(\mathbf{\Omega}_\zeta \zeta)}{\partial \beta}\right|_0 & -\dfrac{1}{2}\,\mathbf{\Omega}_\zeta|_0 & \mathbf{0} & \mathbf{0} \\ \mathbf{0} & \mathbf{0} & \left[\mathbf{C}^{\mathrm{GB}}|_0 \;\; \mathbf{0}\right] & \left.\dfrac{\partial(\mathbf{C}^{\mathrm{GB}}\mathbf{v}_B)}{\partial \zeta}\right|_0 & \mathbf{0} & \mathbf{0} \\ \mathbf{0} & \mathbf{F}_{2F} & \mathbf{F}_{2B} & \mathbf{0} & \mathbf{0} & \mathbf{F}_1 \end{bmatrix} \tag{A.6}$$

$$\mathbf{Q}_3^T = \begin{bmatrix} \mathbf{0} & \left(\left.\dfrac{\partial \mathbf{R}_F^{\mathrm{ctrl}}}{\partial \mathbf{u}}\right|_0\right)^T & \left(\left.\dfrac{\partial \mathbf{R}_B^{\mathrm{ctrl}}}{\partial \mathbf{u}}\right|_0\right)^T & \mathbf{0} & \mathbf{0} & \mathbf{0} \end{bmatrix} \tag{A.7}$$

and

$$\mathbf{Q}_4^T = \begin{bmatrix} \mathbf{0} & \left(\left.\dfrac{\partial \mathbf{R}_F^{\mathrm{aero}}}{\partial \mathbf{w}_g}\right|_0\right)^T & \left(\left.\dfrac{\partial \mathbf{R}_B^{\mathrm{aero}}}{\partial \mathbf{w}_g}\right|_0\right)^T & \mathbf{0} & \mathbf{0} & \mathbf{0} \end{bmatrix}. \tag{A.8}$$

References

[1] C.P. Tilmann, P.M. Flick, C.A. Martin, M.H. Love, High altitude long endurance technologies for sensorcraft, in: NATO/RTO AVT-099 Applied Vehicle Technology Panel (AVT) Symposium on Novel and Emerging Vehicle and Vehicle Technology Concepts, NATO Research and Technology Organization, Brussels, Belgium, 2003, RTO Paper MP-104-P-26.

[2] T.E. Noll, S.D. Ishmael, B. Henwood, M.E. Perez-Davis, G.C. Tiffany, J. Madura, M. Gaier, J.M. Brown, T. Wierzbanowski, Technical findings, lessons learned, and recommendations resulting from the Helios prototype vehicle mishap, in: NATO/RTO AVT-145 Applied Vehicle Technology Panel (AVT) Workshop on UAV Design Processes/Design Criteria for Structures, Florence, Italy, 2007.

[3] M.J. Patil, D.H. Hodges, C.E.S. Cesnik, Nonlinear aeroelastic analysis of complete aircraft in subsonic flow, J. Aircr. 37 (5) (2000) 753–760, https://doi.org/10.2514/2.2685.

[4] M.J. Patil, D.H. Hodges, C.E.S. Cesnik, Nonlinear aeroelasticity and flight dynamics of high-altitude long-endurance aircraft, J. Aircr. 38 (1) (2001) 88–94, https://doi.org/10.2514/2.2738.

[5] E. Livne, T.A. Weisshaar, Aeroelasticity of nonconventional airplane configurations–past and future, J. Aircr. 40 (6) (2003) 1047–1065, https://doi.org/10.2514/2.7217.

[6] C.M. Shearer, C.E.S. Cesnik, Nonlinear flight dynamics of very flexible aircraft, J. Aircr. 44 (5) (2007) 1528–1545, https://doi.org/10.2514/1.27606.

[7] W. Su, C.E.S. Cesnik, Nonlinear aeroelasticity of a very flexible blended-wing-body aircraft, J. Aircr. 47 (5) (2010) 1539–1553, https://doi.org/10.2514/1.47317.

[8] W. Su, C.E.S. Cesnik, Dynamic response of highly flexible flying wings, AIAA J. 49 (2) (2011) 324–339, https://doi.org/10.2514/1.J050496.

[9] D.H. Hodges, E.H. Dowell, Nonlinear equations of motion for elastic bending and torsion of twisted nonuniform blades, Tech. Rep. NASA TN D-7818, National Aeronautics and Space Administration, 1974.

[10] O.A. Bauchau, C.H. Hong, Nonlinear composite beam theory, J. Appl. Mech. 55 (1) (1988) 156–163, https://doi.org/10.1115/1.3173622.

[11] P.F. Pai, Problems in geometrically exact modeling of highly flexible beams, Thin-Walled Struct. 76 (2014) 65–76, https://doi.org/10.1016/j.tws.2013.11.008.

[12] D.H. Hodges, A mixed variational formulation based on exact intrinsic equations for dynamics of moving beams, Int. J. Solids Struct. 26 (11) (1990) 1253–1273, https://doi.org/10.1016/0020-7683(90)90060-9.

[13] D.H. Hodges, Geometrically exact, intrinsic theory for dynamics of curved and twisted anisotropic beams, AIAA J. 41 (6) (2003) 1131–1137, https://doi.org/10.2514/2.2054.

[14] W. Su, C.E.S. Cesnik, Strain-based geometrically nonlinear beam formulation for modeling very flexible aircraft, Int. J. Solids Struct. 48 (16–17) (2011) 2349–2360, https://doi.org/10.1016/j.ijsolstr.2011.04.012.

[15] R. Palacios, J. Murua, R. Cook, Structural and aerodynamic models in nonlinear flight dynamics of very flexible aircraft, AIAA J. 48 (11) (2010) 2648–2659, https://doi.org/10.2514/1.J050513.

[16] M.C. van Shoor, S.H. Zerweckh, A.H. von Flotow, Aeroelastic stability and control of a highly flexible aircraft, in: Proceedings of the 30th AIAA Structures, Structural Dynamics and Materials Conference, Mobile, AL, 1989, AIAA-1989-1187.

[17] M. Drela, Integrated simulation model for preliminary aerodynamic, structural, and control-law design of aircraft, in: Proceedings of the 40th AIAA Structures, Structural Dynamics and Materials Conference, St. Louis, MO, 1999, AIAA-1999-1394.

[18] M. Drela, Aswing aerodynamics structures control configuration development system for flexible aircraft, https://web.mit.edu/drela/Public/web/aswing/, 2010.

[19] D.A. Peters, M.J. Johnson, Finite-state airloads for deformable airfoils on fixed and rotating wings, in: P.P. Friedmann, J.C.I. Chang (Eds.), Symposium on Aeroelasticity and Fluid/Structure Interaction, in: ASME Winter Annual Meeting, vol. AD-44, American Society of Mechanical Engineers, New York, NY, 1994, pp. 1–28.

[20] D.A. Peters, S. Karunamoorthy, W.-M. Cao, Finite state induced flow models part I: two-dimensional thin airfoil, J. Aircr. 32 (2) (1995) 313–322, https://doi.org/10.2514/3.46718.

[21] D.A. Peters, C.-J. He, Finite state induced flow models part II: three-dimensional rotor disk, J. Aircr. 32 (2) (1995) 323–333, https://doi.org/10.2514/3.46719.

[22] M.J. Patil, D.H. Hodges, Flight dynamics of highly flexible flying wings, J. Aircr. 43 (6) (2006) 1790–1799, https://doi.org/10.2514/1.17640.

[23] J. Murua, R. Palacios, J.M.R. Graham, Applications of the unsteady vortex-lattice method in aircraft aeroelasticity and flight dynamics, Prog. Aerosp. Sci. 55 (2012) 46–72, https://doi.org/10.1016/j.paerosci.2012.06.001.

[24] J. Zeng, B. Moulin, R. de Callafon, M.J. Brenner, Adaptive feedforward control for gust load alleviation, J. Guid. Control Dyn. 33 (3) (2010) 862–872, https://doi.org/10.2514/1.46091.

[25] X. Liu, Q. Sun, J.E. Cooper, LQG based model predictive control for gust load alleviation, Aerosp. Sci. Technol. 71 (2017) 499–509, https://doi.org/10.1016/j.ast.2017.10.006.

[26] X. Wang, E.V. Kampen, Q.P. Chu, R. de Breuker, Flexible aircraft gust load alleviation with incremental nonlinear dynamic inversion, J. Guid. Control Dyn. 42 (7) (2019) 1519–1536, https://doi.org/10.2514/1.G003980.

[27] A. Khalil, N. Fezans, Gust load alleviation for flexible aircraft using discrete-time h_∞ preview control, Aeronaut. J. 125 (1284) (2021) 341–364, https://doi.org/10.1017/aer.2020.85.

[28] S. Haghighat, H.H.T. Liu, J.R.R.A. Martins, Model-predictive gust load alleviation controller for a highly flexible aircraft, J. Guid. Control Dyn. 35 (6) (2012) 1751–1766, https://doi.org/10.2514/1.57013.

[29] R.G. Cook, R. Palacios, P. Goulart, Robust gust alleviation and stabilization of very flexible aircraft, AIAA J. 51 (2) (2013) 330–340, https://doi.org/10.2514/1.J051697.

[30] M.S. Spillman, Robust longitudinal flight control design using linear parameter-varying feedback, J. Guid. Control Dyn. 23 (1) (2000) 101–108, https://doi.org/10.2514/2.4492.

[31] J.M. Barker, G.J. Balas, Comparing linear parameter-varying gain-scheduled control techniques for active flutter suppression, J. Guid. Control Dyn. 23 (5) (2000) 948–955, https://doi.org/10.2514/2.4637.

[32] R. Lind, Linear parameter-varying modeling and control of structural dynamics with aerothermoelastic effects, J. Guid. Control Dyn. 25 (4) (2002) 733–739, https://doi.org/10.2514/2.4940.

[33] T. He, G. Zhu, S.S.-M. Swei, W. Su, Smooth-switching LPV control for vibration suppression of a flexible airplane wing, Aerosp. Sci. Technol. 84 (2019) 895–903, https://doi.org/10.1016/j.ast.2018.11.029.

[34] S. Snyder, P. Zhao, N. Hovakimyan, Adaptive control for linear parameter-varying systems with application to a VTOL aircraft, Aerosp. Sci. Technol. 112 (2021) 106621, https://doi.org/10.1016/j.ast.2021.106621.

[35] J. Hanema, M. Lazar, R. Tóth, Stabilizing tube-based model predictive control: terminal set and cost construction for LPV systems, Automatica 85 (2017) 137–144, https://doi.org/10.1016/j.automatica.2017.07.046.

[36] J. Hanema, M. Lazar, R. Tóth, Heterogeneously parameterized tube model predictive control for LPV systems, Automatica 111 (2020) 108622, https://doi.org/10.1016/j.automatica.2019.108622.

[37] R. Song, Z. Ye, L. Wang, T. He, L. Zhang, Autonomous wheel loader trajectory tracking control using LPV-MPC, arXiv:2203.08944, 2022.

[38] S. Qu, G. Zhu, W. Su, S.S.-M. Swei, Linear parameter-varying-based transition flight control design for a tilt-rotor aircraft, Proc. Inst. Mech. Eng., G J. Aerosp. Eng. 236 (16) (2022) 3354–3369, https://doi.org/10.1177/09544100221083713.

[39] A. Iannelli, U. Fasel, R.S. Smith, The balanced mode decomposition algorithm for data-driven LPV low-order models of aeroservoelastic systems, Aerosp. Sci. Technol. 115 (2021) 106821, https://doi.org/10.1016/j.ast.2021.106821.

[40] Z. Gu, S. Pang, Y. Li, Q. Li, Y. Zhang, Turbo-fan engine acceleration control schedule optimization based on DNN-LPV model, Aerosp. Sci. Technol. 128 (2022) 107797, https://doi.org/10.1016/j.ast.2022.107797.

[41] A. Kapnopoulos, A. Alexandridis, A cooperative particle swarm optimization approach for tuning an MPC-based quadrotor trajectory tracking scheme, Aerosp. Sci. Technol. 127 (2022) 107725, https://doi.org/10.1016/j.ast.2022.107725.

[42] S. Samsam, R. Chhabra, Nonlinear model predictive control of J2-perturbed impulsive transfer trajectories in long-range rendezvous missions, Aerosp. Sci. Technol. 132 (2023) 108046, https://doi.org/10.1016/j.ast.2022.108046.

[43] W.A. Silva, Simultaneous excitation of multiple-input/multiple-output CFD-based unsteady aerodynamic systems, J. Aircr. 45 (4) (2008) 1267–1274, https://doi.org/10.2514/1.34328.

[44] W.A. Silva, AEROM: NASA's unsteady aerodynamic and aeroelastic reduced-order modeling software, Aerospace 5 (2) (2018) 41, https://doi.org/10.3390/aerospace5020041.

[45] P. Towers, B.L. Jones, Real-time wind field reconstruction from LiDAR measurements using a dynamic wind model and state estimation, Wind Energy 19 (1) (2016) 133–150, https://doi.org/10.1002/we.1824.

[46] E.F. Camacho, C. Bordons, Model Predictive Control: Classical, Robust and Stochastic, Advanced Textbooks in Control and Signal Processing, Springer International Publishing, Switzerland, 2016.

[47] P.S.G. Cisneros, H. Werner, Parameter-dependent stability conditions for quasi-LPV model predictive control, in: 2017 American Control Conference (ACC), 2017, pp. 5032–5037.

[48] D.J. Moorhouse, R.J. Woodcock, Background information and user guide for MIL-F-8785C, military specification - flying qualities of piloted airplanes, Tech. Rep. ADA119421, US Air Force Systems Command, Wright-Patterson AFB, OH, 1982.

[49] W. Su, S.S.-M. Swei, G. Zhu, Optimum wing shape of highly flexible morphing aircraft for improved flight performance, J. Aircr. 53 (5) (2016) 1305–1316, https://doi.org/10.2514/1.C033490.

[50] A.K. Al-Jiboory, G. Zhu, S.S.-M. Swei, W. Su, N.T. Nguyen, LPV modeling of a flexible wing aircraft using modal alignment and adaptive gridding methods, Aerosp. Sci. Technol. 66 (2017) 92–102, https://doi.org/10.1016/j.ast.2017.03.009.

[51] A. Gupta, M. Mejari, P. Falcone, D. Piga, Computation of parameter dependent robust invariant sets for LPV models with guaranteed performance, Automatica 151 (2023) 110920, https://doi.org/10.1016/j.automatica.2023.110920.